ORIGINAL PAPER

physica status solidi b

www.pss-b.com

Dynamic Impurity Redistributions in Kesterite Absorbers

Sigbjørn Grini, Hisham Aboulfadl, Nils Ross, Clas Persson, Charlotte Platzer-Björkman, Mattias Thuvander, and Lasse Vines*

$Cu_2ZnSn(S,Se)_4$ is a promising nontoxic earth-abundant solar cell absorber. To optimize the thin films for solar cell device performance, postdeposition treatments at temperatures below the crystallization temperature are normally performed, which alter the surface and bulk properties. The polycrystalline thin films contain relatively high concentrations of impurities, such as sodium, oxygen and hydrogen. During the treatments, these impurities migrate and likely agglomerate at lattice defects or interfaces. Herein, impurity redistribution after air annealing for temperatures up to 200 °C and short heavy water treatments are studied. In addition, nonuniformities of the sodium distribution on a nanometer and micrometer scale are characterized by atom probe tomography and secondary ion mass spectrometry, respectively. Sodium and oxygen correlate to a greater extent after heat treatments, supporting strong binding between the two impurities. Redistributions of these impurities occur even at room temperature over longer time periods. Heavy water treatments confirm out-diffusion of sodium with more incorporation of oxygen and hydrogen. It is observed that the increased hydrogen content does not originate from the heavy water. The existence of an "ice-like" layer on top of the Cu_2ZnSnS_4 layer is proposed.

1. Introduction

Impurities are of vital importance for the performance of semiconductor devices.[1,2] This holds particularly true for $Cu_2ZnSn(S,Se)_4$ (called CZTSSe or kesterite), a promising absorber material for solar cell applications. For CZTSSe thin films, there are not only several intrinsic defects,[3] but also many extrinsic impurities such as sodium (Na), oxygen (O), and hydrogen (H). Na is intentionally introduced via the soda-lime glass (SLG) substrate, or added during the fabrication process, for instance, through NaF treatment.[4] Na has been proposed to passivate grain boundaries and deep defects, increase the carrier concentration and contribute to crystal growth of CZTSSe.[4–7] Na has been commonly observed not only to segregate at the grain boundaries, but also a significant amount usually resides inside the grains at other defect types.[8] In addition, cluster formations have been observed.[9,10] Other alkalis may also be added and yield a positive effect on the device performance.[11] Oxygen, on the contrary, is unintentionally introduced into CZTSSe and may originate from the Mo layer and through contaminations during the processing.[12] O has been observed in grain boundaries and on the surface, either correlated with Na[13] or as SnO_x[14,15] Hydrogen has also been reported to have a passivating effect.[16]

It is well known that air annealing of CZTSSe samples during processing can improve the power conversion efficiency (PCE). However, air annealing at certain temperatures may also be detrimental for the PCE. Air annealing is typically performed below the crystallization temperature and the effects on the performance can be attributed to redistribution of impurities[15,17,18] or modification of the surface.[19,20] If the PCE improvements are related to the former, the diffusion mechanisms of the involved are of utmost importance. Na diffusion has been extensively studied in Cu(In,Ga)Se_2,[21–24] however, less is known about the diffusion in CZTSSe.[17,18] To the best of our knowledge, no study has been dedicated to study diffusivity of O in kesterite thin films. We have previously identified the correlation between Na and O in Cu_2ZnSnS_4 (CZTS) and shown that O can be used to trap Na due to the strong Na—O bond.[25] Therefore, a necessary aspect is to study Na and O depth profiles after

Dr. S. Grini, Dr. N. Ross, Prof. C. Persson, Prof. L. Vines
Department of Physics/Centre for Materials Science and Nanotechnology
University of Oslo
P.O. Box 1048, Blindern, N-0316 Oslo, Norway
E-mail: sigbjorn.grini@smn.uio.no

The ORCID identification number(s) for the author(s) of this article can be found under https://doi.org/10.1002/pssb.202000062.

DOI: 10.1002/pssb.202000062

Dr. H. Aboulfadl, Prof. M. Thuvander
Department of Physics
Chalmers University of Technology
41296 Göteborg, Sweden

Dr. N. Ross, Prof. C. Platzer-Björkman
Ångström Solar Center
Division of Solid State Electronics
Uppsala University
Uppsala 75120, Sweden

Prof. C. Persson
Department of Materials Science and Engineering
KTH Royal Institute of Technology
10044 Stockholm, Sweden

low-temperature heat treatments, which can reveal their diffusion mechanisms.

Here, we report on the redistribution of three prevalent impurities in CZTS during air annealing and wet chemical treatments. To better distinguish diffusion inside grains and at grain boundaries, one can vary the average size of the grains. To accomplish this, we prepared two sample sets of sulfide CZTS on top of Mo where we varied the sulfurization time from 10 to 40 min at a lower-than-baseline temperature of 500 °C resulting in a total of six samples (a–f). The average grain sizes were estimated to vary between roughly 100 nm for sample (a) to 300 nm for sample (f). Fortuitously, after the sulfurization a nonuniform Na and O distribution with depth was produced for all samples (shown later). With isothermal air annealing treatments from 50 to 200 °C, Na and O diffuse in the CZTS absorbers. In addition, postdeposition "wet chemical cleaning" treatments are commonly used to remove unwanted phases on the surface of the CZTS absorber before the buffer layer deposition.[11,26,27] Water (H_2O) treatments can remove such phases.[28] The origin of the H in-diffusion is evaluated by using heavy water (D_2O) treatments.

2. Results and Discussion

2.1. Spatial Nonuniformity of Na in Cu_2ZnSnS_4

Spatial variations of sodium are prevalent in the samples of this study, in agreement with previous studies on CZTSSe.[9,10,29–31] **Figure 1** shows the spatial sodium distribution of two CZTS absorber specimens on the nanometer and micrometer scale using atom probe tomography (APT) and secondary ion mass spectrometry (SIMS) image depth profiling. Two tomographic slices of the 3D reconstruction of the APT-tip (Figure 1a,c) highlight the Na spatial distribution's nonuniformity. Segregations to clusters and dislocations were observed in the grain interior, as shown in Figure 1a,c. A 2D defect is also observed at the upper left part of the reconstruction which exhibits Na agglomeration. Solely from the APT data, the nature of 2D defects cannot be identified, which here could be either a grain boundary or a stacking fault. The APT reconstruction volume exhibits several features which display not only Na segregations, but also Cu inhomogeneities, as shown in Figure 1b. A 2D concentration map for the Cu concentration within a tomographic slice in

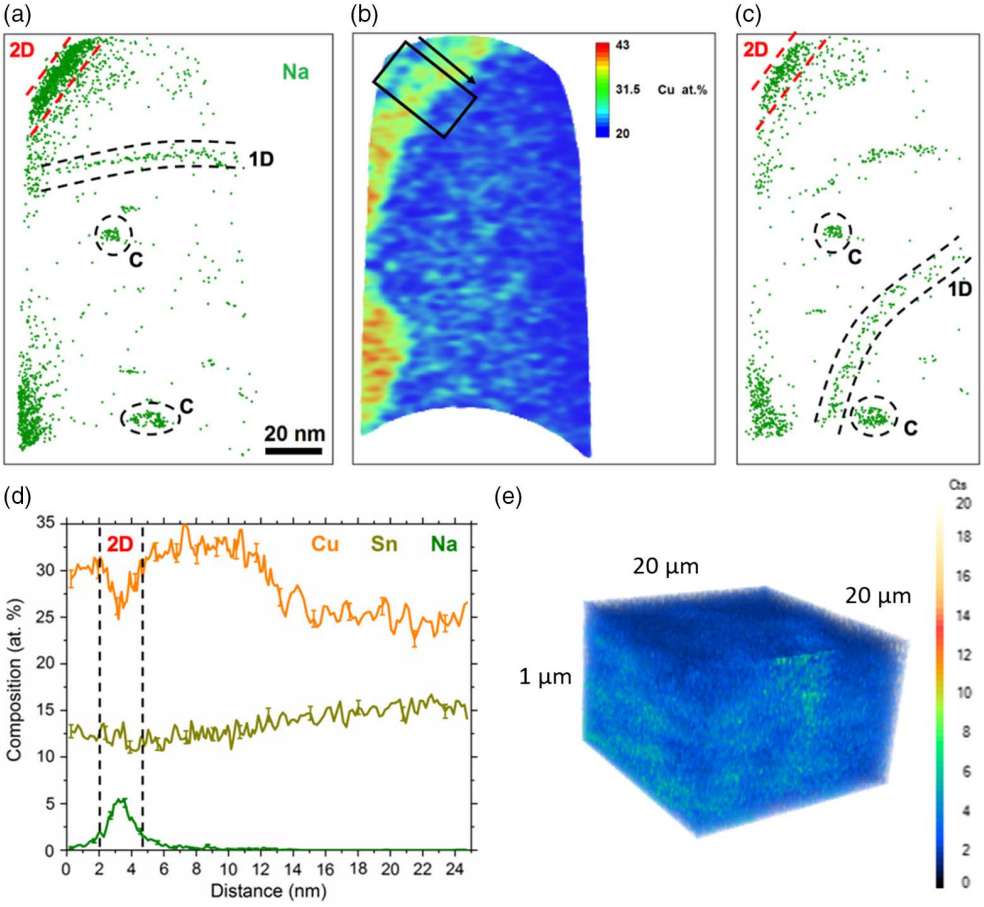

Figure 1. Sodium distribution on a–d) the nanometer scale using APT and on e) the micrometer scale using SIMS image depth profile. a,c) Two tomographic slices of 8 nm thickness within the point cloud data representing Na atoms. Clusters are marked by "C," decorated dislocations are marked by "1D" and the 2D lattice defect is marked by "2D," respectively. b) A 2D concentration map for the Cu concentration from within the same slice of part (a). d) 1D concentration profile across the 2D defect, the region is marked by a black rectangle in part (b), the arrow marks the direction of the profile measurement.

the point cloud reconstruction highlights the inhomogeneity of Cu. Figure 1d shows a profile across the 2D defect (marked with a rectangle in Figure 1b). Concentrations and distribution of Zn, S, and O are not presented here due to interference with other elements and/or molecules (see Section 4). At the 2D defect, a strong increase in Na concentration is observed, reaching up to ≈6 at%, as well as a clear depletion of Cu. It has been shown by Schwarz et al. using APT that alkali rich grain boundaries in selenide $Cu_2ZnSnSe_4$ (CZTSe) can sometimes display Cu segregations or Cu depletion.[10] This has also been reported for $Cu(In,Ga)Se_2$ absorbers.[32] Changes in the matrix elements at the grain boundaries are argued to influence the electrical performance of the planar defects in the polycrystalline structures where such defects can be beneficial or detrimental to the device performance.[33] Depletion of Cu at the $Cu(In,Ga)(S,Se)_2$ and $CuInSe_2$ grain boundaries is, however, suggested to create hole barriers, reducing recombination effects.[34] It is important to mention, however, that the Na concentration at the planar defect here is relatively high which suggests the formation of a secondary phase containing Na.

At the proximity of the planar interface, the Cu concentration is seen to rise ≈6 at% above the average concentration detected at further distances (in the grain interior). In principle, inhomogeneity of absorber main elements in CZTS is expected because the system exhibits strong tendencies of secondary phase formation due to the narrow compositional range of CZTS.[35] The high diffusivity of Cu in the compound is argued to facilitate the nucleation of $Cu_{2-x}Se$ phases in CZTSe,[36,37] which are commonly observed at the absorber surface and near grain boundaries.[38] Investigations using in situ heating in a scanning electron transmission microscope have shown that this is influenced by migration of grain boundaries.[39] Therefore, the Cu enrichment observed here near a planar defect in the CZTS absorber is likely to be due to high Cu diffusion during film growth and the general tendency of $Cu_2S(Se)$ formation in this system at grain boundaries.

At the proximity of the planar defect where Cu concentration was found to be higher, a slight increase in Na (≈0.5 at%) is also detected, which is predicted to be caused by out-diffusion of the Na segregated at the planar defect. Other areas in the reconstruction show similar behavior (i.e., bottom left region in Figure 1b) of Na and Cu inhomogeneities that are correlated at the same regions, which is expected to be caused by the same mechanism stemming from migrating lattice defects in the absorber. However, further investigations are required to reveal such mechanisms, but this is outside the scope of the current work.

SIMS image depth profile measurements of Na reveal a nonuniform spatial distribution of the SIMS intensity on the micrometer scale (Figure 1e). The nonuniformity is present both laterally with a $20 \times 20\ \mu m^2$ raster and throughout the depth of the 1 μm-thick CZTS layer, indicating that the Na-rich regions are not limited to regions on a nanometer scale. In fact, inhomogeneities of Na on a millimeter scale has also been observed by performing SIMS at several locations (not shown). This has already been identified by Gershon et al. and has been attributed to inhomogeneities in the SLG.[31] To limit the effects of these inhomogeneities, SIMS depth profiles are measured as close as possible to each other after heat treatments and heavy water treatments.

2.2. Redistribution of Na and O

Six samples with different grain sizes were annealed on a hot plate in air at 50, 100, 150, and 200 °C for 30 min. For each sample, SIMS depth profiles were measured, and elastic recoil detection analysis (ERDA)-calibrated Na and O concentrations were estimated. The results are shown in **Figure 2** and **3**, where the estimated average grain size for each sample increases from about 100 nm for (a) to about 300 nm for (f). Initially, the depth profiles (blue lines) display an average estimated concentration of Na and O for all samples between 1×10^{19} and 1×10^{20} atoms cm^{-3}, showing no correlation between measured concentration with SIMS and the grain size. However, the Na and O concentrations correlate for all samples over all temperatures. The concentrations are increased at the air/surface and the CZTS/Mo interfaces for all samples, indicating segregation of Na and O at these interfaces.[40] The increased SIMS intensity may also be caused by a change in sputter yield and ionization efficiency at these interfaces, making quantitative assessment challenging.[41] To a greater extent than that of O, accumulation of Na is observed in the regions from 600 to 900 nm from the surface, near the back contact. This accumulation of Na after the sulfurization is not commonly observed in conventional CZTS samples. Different from conventional processing, these samples are processed at lower-than-baseline temperatures of about 500 °C and with a longer sulfurization time to induce more variation in grain size between samples. The unconventional sulfurization conditions may have caused the abnormal Na accumulation in the region near the back contact for all samples studied. As the samples are air annealed, Na appears to diffuse from this region and redistributes to sites closer to the surface. Indeed, after the 100 and 150 °C anneals, each sample exhibited a substantially more uniform Na distribution with depth. While Na redistributes in the CZTS layer, Na from the SLG is expected to act as a source and diffuse through the Mo at these temperatures,[17,42] which could explain the increased Na concentration for all depths as observed in (c) and (d). Evidently, the extent of the redistribution of Na after the 50 °C anneal correlates with grain size, suggesting that diffusion through grain boundaries are preferred, as expected. However, the Na concentrations for the sample with the smallest grain size (a) do not redistribute further at higher temperatures. In fact, the sample with the smallest grain size has the lowest overall concentration of Na in the CZTS layer after heat treatments of the six samples, suggesting that the Na occupies sites inside the grain interior. The O depth profiles (Figure 3) show that the O concentration is increased for all samples after heat treatments to a larger extent than that of Na. Indeed, the depth profiles and concentration levels are much more similar after air annealing treatments. The similar depth profiles compared with that prior to annealing may come as a result of formation Na–O complexes in the absorber.[12]

From Figure 2, significant Na redistribution and an increase in O concentration are observed after the heat treatments. The rapid diffusion of Na at low temperatures suggests that Na may be mobile at or slightly above room temperature. In this case, long-term storage at room temperature would be sufficient for Na to migrate. Therefore, a reference piece from the sample (e) was measured 276 days after the initial SIMS measurement.

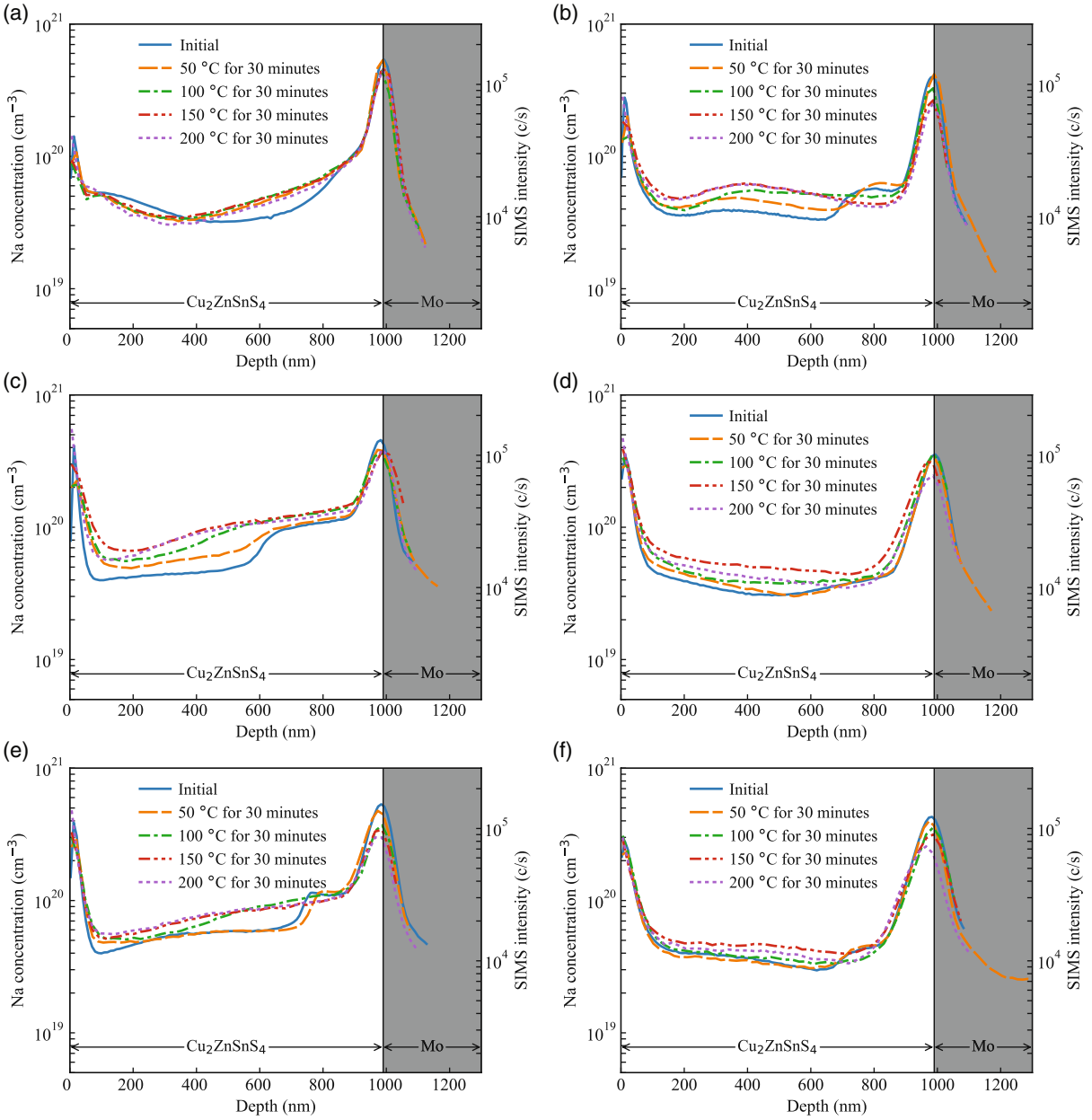

Figure 2. ERDA calibrated SIMS Na depth profiles for six samples (a–f) initially and after air annealing treatments at 100, 150, and 200 °C for 30 min. The average CZTS grain size increases from about 100 nm to about 300 nm in the samples from (a) to (f).

The measured depth profiles and the initial depth profiles are shown in **Figure 4**. Clearly, Na and O have redistributed over the depth of the CZTS layer after long-term storage confirming the low migration barrier for Na in CZTS. The depth profile is remarkably similar to that of the depth profiles measured after the 150 °C air anneal, proposing that the long-term storage has similar effects on the Na and O distributions as the short anneals at elevated temperatures. The similarity between Na and O depth profiles might be indicative of comparable solar cell properties. Thus, an interesting study would be to explore whether long-term storage in air before the buffer layer deposition produces effects on PCE comparable with shorter low-temperature air anneals.

2.3. Impurity Migration after Heavy Water Treatment

Water treatments have been shown to remove Na and O on the surface.[28] Indeed, a reference SIMS measurement of a CZTS absorber treated in regular deionized water (H_2O) indicated out-diffusion of Na from the bulk (not shown). A likely candidate to replace Na is H. Thus, to distinguish possible in-diffusion of H from the water with the H in the air and that already present in the CZTS, samples from a third series were treated in heavy water (D_2O) for 40 s and SIMS depth profiles of Na, O, H, and D were measured before and directly after the procedure. **Figure 5** shows the depth profiles from a representative sample of the four

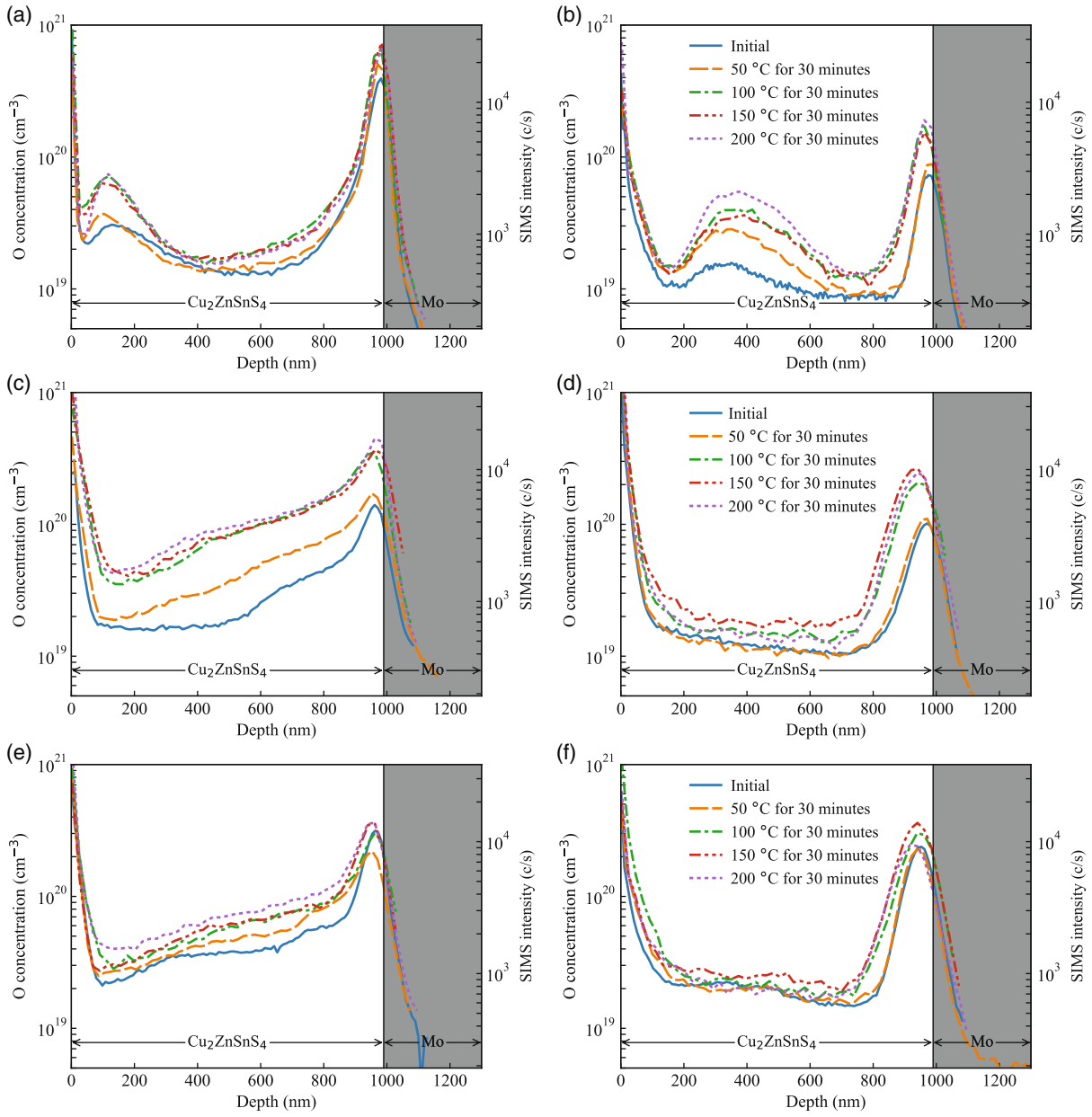

Figure 3. ERDA calibrated SIMS O depth profiles for six samples (a–f) initially and after air annealing treatments at 100, 150, and 200 °C for 30 min. The average CZTS grain size increases from about 100 nm to about 300 nm in the samples from (a) to (f).

species before (solid lines) and after (dashed lines) the D_2O treatment. The Na intensity has decreased, most noticeably in the region near the surface. The H intensity, meanwhile, has increased after the D_2O treatment with more H introduced in the near-surface region, correlating inversely with Na suggesting a kick-out of Na by H. A significant signal from D is observed after the D_2O treatment, although it is several orders of magnitude lower than the increase in H. Although the intensity of D is low compared with that of H, the diffusion is fast as D is detected throughout the CZTS absorber and into the Mo back contact. Interestingly, the SIMS intensity from D was equal for all samples regardless of grain size, indicating that the sites occupied by D are not limited to grain boundaries.

Surprisingly, the increase in SIMS intensity for H is greater than for D after the D_2O treatment. The immediate possible source of H is from H_2O in the ambient air. The in-diffusion of H would be expected to occur during the D_2O dip where the out-diffusion of Na most likely occurs. Interestingly, a similar observation has been reported in porous materials, where an "ice-like" layer has been identified with conductivity measurements.[43–45] The thickness of the layer was governed by the humidity when exposed to air. Thus, one may propose a similar explanation to why limited amounts of D diffuse from the D_2O during the 40 s treatment, i.e., that an "ice-like" layer of H_2O is formed on top of the CZTS. While speculative, the CZTS sample shown in Figure 5 was exposed to air during

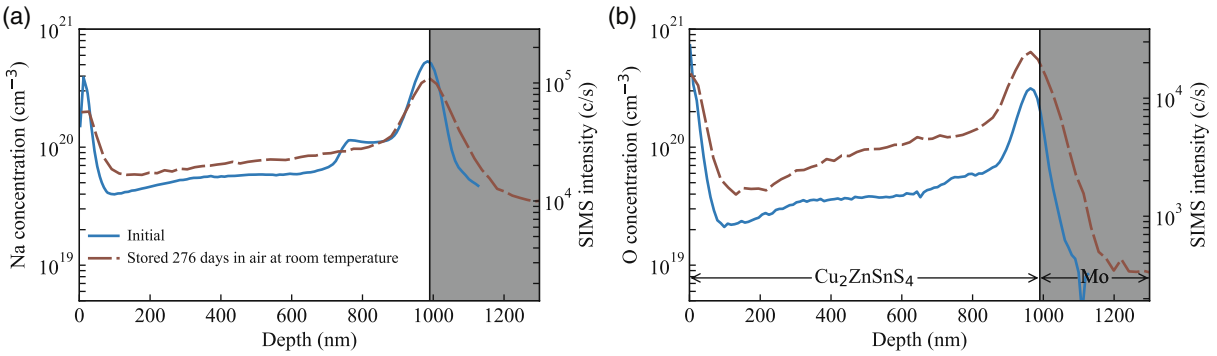

Figure 4. a) Na and b) O concentrations measured by SIMS for sample (e) from Figure 2 initially and after the sample was stored at room temperature for 276 days. The Na and O depth profiles after storage (dashed lines) are comparable to what was observed after the 150 °C air annealing treatment (Figure 2e).

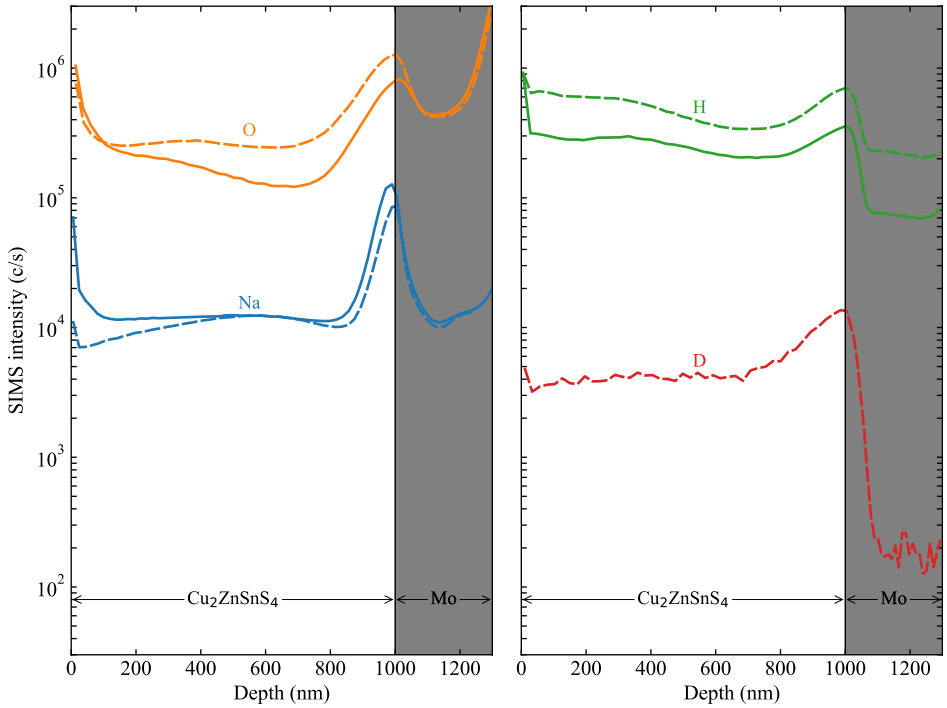

Figure 5. SIMS measurements of Na, O, H, and D (deuterium) on a representative CZTS absorber before (solid lines) and after (dashed lines) the sample has been treated in D_2O for 40 s. The elements are separated in two plots for easier interpretation. A decrease in the Na intensity and an increase in the O and H intensities are observed. Trace amounts of D have diffused from the D_2O into the CZTS and the Mo layer.

transport and storage, supporting that such a layer could form. Accordingly, the H from the "ice-like" layer diffuses in and exchanges sites with Na, much like the proposed diffusion of Na from the SLG to the CZTS layer. The "ice-like" layer may also act as a source for O, even though the increase is more significant near the Mo back contact.

3. Conclusion

Nonuniform Na distributions on the nanometer and micrometer scale have been identified in our CZTS samples by APT and SIMS image depth profile measurements. The APT analysis reveals that Na is accumulated at lattice defects in the absorber and forming clusters. It has also shown that Cu has a higher concentration near the planar defects possibly related to high Cu diffusivity and grain boundary migration. Furthermore, redistribution of Na and O have been observed after air annealing at temperatures up to 200 °C for CZTS samples with varying average grain size. The low migration barriers for Na and O allow for redistribution of these impurities to occur, even at room temperature. The diffusion of impurities in CZTS is likely grain boundary mediated, however, the redistribution appears to occur at sites in the grain interior. The out-diffusion of Na and the in-diffusion of H are identified by treatment in D_2O, demonstrating that water treatments do not only remove Na from the surface. It is proposed that

the increase in H in contrast to D could be explained by an existing "ice-like" layer on the CZTS surface preventing abundant amounts of D to diffuse into the sample during the D_2O treatment.

4. Experimental Section

The Mo (99.97% purity) bilayer was DC sputtered on top of SLG substrates with Ar (99.9995% purity) as the sputtering gas. No extra sodium was added at this stage, nor any diffusion barrier was used. CuS, ZnS, and SnS precursors (all 99.99% purity) were cosputtered using a Lesker CMS-18 sputter system. The precursors were sputtered with a 666 Pa Ar background pressure at a substrate temperature of 250 °C. Sulfurization was performed with 80 mg of sulfur in a pyrolytic carbon-coated graphite box in a tube furnace at 500 ± 10 °C for 10, 20, and 40 min for two sample sets. The precursor compositions were determined with Rutherford backscattering-calibrated X-ray fluorescence measurements and the average grain sizes were estimated by counting the number of grain boundaries over a line and dividing by the length of the line using top-view SEM images. The grain size and morphology of a similar sample set had been discussed previously.[46] The sample sets had both a [Cu]/[Sn] = 1.92, with dissimilar [Zn]/([Sn] + [Cu]) of 0.32 (samples (a), (c), and (e)) and 0.35 (samples (b), (d), and (f)), respectively. Isothermal heat treatments were performed on the samples using a hot plate at 50, 100, 150, and 200 °C for 30 min each in air ambience. Samples from a third sample set were treated in room tempered heavy water (D_2O) by dipping and holding them for 40 s. All samples were characterized with SIMS using a Cameca IMS 7f magnetic sector instrument before and after the treatments. Cs^+ primary ions were utilized. For estimation of Na and O concentrations from the air annealing series, the cluster ions $^{23}Na^{133}Cs^+$ and $^{16}O^{133}Cs^+$ were detected and calibrated against a time-of-flight-energy elastic recoil detection analysis (ToF-ERDA) reference sample using the $^{98}Mo^{133}Cs^+$ signal in the Mo layer to produce the relative sensitivity factor. The ToF-ERDA measurement was performed using I^{8+} primary ions with an impact energy of 36 MeV. The impinging ions covered an area of a few millimeters, which is substantially larger compared with SIMS such that the estimated concentrations are considered to be indicative. For the samples treated in D_2O, the negative ions $^1H^-$, $^2H^-$ (D^-), and $^{18}O^-$ were also detected. The matrix signal detected for the negative ions was $^{120}Sn^-$, however, variations in the Sn signal for the reference sample was observed leading to uncertainties in the concentration estimation, and thus, only the SIMS intensity is presented. Cs^+ impact energies were 15 and 5 keV for negative and positive secondary ions, respectively. The beam was always rastered over an area of 150 × 150 μm^2 collecting secondary ions from a circular region in the middle of the crater with diameter of 33 μm. The primary beam current was 20 nA. The depth of the CZTS layer was estimated by comparing with cross-sectional SEM images and the CZTS/Mo interface was defined by the inflection point of the Mo signal. For SIMS image depth profiling, O_2^+ primary ions with 10 keV impact energy using a beam current of 100 pA were utilized for increased spatial resolution. One sample from the first sample set was chosen for APT analysis with the goal of studying the Na distribution on a finer scale. APT specimens were prepared using a dual-beam focused ion-beam/scanning electron microscopy (FIB/SEM) workstation (FEI Versa 3D). A standard lift-out technique was implemented for specimen preparation,[47] having the main axis of the needle-shaped specimens oriented perpendicular to the substrate. An approximately 200 nm-thick Pt layer was deposited on top, using the electron beam as a protective coating. Furthermore, 2 kV acceleration voltage was used for the final shaping of the specimens to reduce Ga implantation. APT measurements were carried out in a LEAP 3000X-HR (Imago) system in laser pulsing mode with a repetition rate of 100 kHz, 0.05 nJ laser power, and base temperature of ≈50 K. The data were reconstructed and analyzed using CAMECA IVAS 3.6.14 software. Analyzing sulfide CZTS with APT was accompanied with some limitations in the composition quantifications stemming from peak overlaps in the mass spectrum for sulfur, oxygen, and zinc elements, respectively. The overlaps occurred at the peaks at 16 Da for $^{32}S^{+2}$ and $^{16}O^{+1}$, at 32 Da for $^{32}S^{+1}$, $^{16}O_2{}^{+1}$, and $^{64}Zn^{+2}$, as well as at 34 Da for $^{34}S^{+1}$ and $^{68}Zn^{+2}$. Correction using natural isotope abundance ratios was rather difficult, especially for the 32 Da peak.[48] Therefore, the chemical quantification using this technique will only focus here on Na, Cu and Sn.

Acknowledgements

This work was funded by the Research Council of Norway (project 243642) and the Swedish Foundation for Strategic Research. The Research Council of Norway is also acknowledged for the support to the Norwegian Micro and Nano-Fabrication Facility, NorFab, project number 245963/F50.

Conflict of Interest

The authors declare no conflict of interest.

Keywords

air annealing, CZTS, impurities, kesterite, oxygen, sodium, solar cell absorber

Received: January 29, 2020
Revised: March 19, 2020
Published online: April 6, 2020

[1] R. Scheer, H. W. Schock, *Chalcogenide Photovoltaics: Physics, Technologies, and Thin Film Devices*, Wiley-VCH, Weinheim, Germany **2011**.
[2] S. M. Sze, M. K. Lee, *Semiconductor Devices, Physics and Technology*, Wiley, Hoboken, NJ **2012**.
[3] S. Chen, A. Walsh, X.-G. Gong, S.-H. Wei, *Adv. Mater.* **2013**, *25*, 1522.
[4] P. M. P. Salomé, H. Rodriguez-Alvarez, S. Sadewasser, *Sol. Energy Mater. Sol. Cells* **2015**, *143*, 9.
[5] C. M. Sutter-Fella, J. A. Stückelberger, H. Hagendorfer, F. La Mattina, L. Kranz, S. Nishiwaki, A. R. Uhl, Y. E. Romanyuk, A. N. Tiwari, *Chem. Mater.* **2014**, *26*, 1420.
[6] T. Prabhakar, N. Jampana, *Sol. Energy Mater. Sol. Cells* **2011**, *95*, 1001.
[7] K. Sun, F. Liu, C. Yan, F. Zhou, J. Huang, Y. Shen, R. Liu, X. Hao, *Sol. Energy Mater. Sol. Cells* **2016**, *157*, 565.
[8] S. Tajima, R. Asahi, D. Isheim, D. N. Seidman, T. Itoh, K. Ohishi, *Jpn. J. Appl. Phys.* **2015**, *54*, 112302.
[9] C. Yan, J. Huang, K. Sun, S. Johnston, Y. Zhang, H. Sun, A. Pu, M. He, F. Liu, K. Eder, L. Yang, J. M. Cairney, N. J. Ekins-Daukes, Z. Hameiri, J. A. Stride, S. Chen, M. A. Green, X. Hao, *Nat. Energy* **2018**, *3*, 764.
[10] T. Schwarz, A. Redinger, S. Siebentritt, Z. Peng, B. Gault, D. Raabe, P. Choi, *Phys. Rev. Mater.* **2019**, *3*, 035402.
[11] S. G. Haass, M. Diethelm, M. Werner, B. Bissig, Y. E. Romanyuk, A. N. Tiwari, *Adv. Energy Mater.* **2015**, *5*, 1500712.
[12] S. Grini, K. V. Sopiha, N. Ross, X. Liu, T. S. Bjørheim, C. Platzer-Björkman, C. Persson, L. Vines, *Adv. Energy Mater.* **2019**, *9*, 1900740.
[13] R. Haight, X. Shao, W. Wang, D. B. Mitzi, *Appl. Phys. Lett.* **2014**, *104*, 033902.
[14] K. Sardashti, R. Haight, T. Gokmen, W. Wang, L.-Y. Chang, D. B. Mitzi, A. C. Kummel, *Adv. Energy Mater.* **2015**, *5*, 1402180.
[15] K. Sardashti, D. Paul, C. Hitzman, J. Hammond, R. Haight, A. C. Kummel, *J. Mater. Res.* **2016**, *31*, 3473.
[16] J. Park, J. Huang, J. Yun, F. Liu, Z. Ouyang, H. Sun, C. Yan, K. Sun, K. Kim, J. Seidel, S. Chen, M. A. Green, X. Hao, *Adv. Energy Mater.* **2018**, *8*, 1701940.

[17] H. Xie, S. López-Marino, T. Olar, Y. Sánchez, M. Neuschitzer, F. Oliva, S. Giraldo, V. Izquierdo-Roca, I. Lauermann, A. Pérez-Rodríguez, E. Saucedo, *ACS Appl. Mater. Interfaces* **2016**, *8*, 5017.
[18] D. Hironiwa, N. Sakai, T. Kato, H. Sugimoto, Z. Tang, J. Chantana, T. Minemoto, *Thin Solid Films* **2015**, *582*, 151.
[19] J. K. Larsen, Y. Ren, N. Ross, E. Särhammar, S.-Y. Li, C. Platzer-Björkman, *Thin Solid Films* **2017**, *633*, 118.
[20] M. Neuschitzer, Y. Sanchez, T. Olar, T. Thersleff, S. Lopez-Marino, F. Oliva, M. Espindola-Rodriguez, H. Xie, M. Placidi, V. Izquierdo-Roca, I. Lauermann, K. Leifer, A. Pérez-Rodriguez, E. Saucedo, *Chem. Mater.* **2015**, *27*, 5279.
[21] A. Laemmle, R. Wuerz, T. Schwarz, O. Cojocaru-Mirédin, P. Choi, M. Powalla, *J. Appl. Phys.* **2014**, *115*, 154501.
[22] R. V. Forest, B. E. McCandless, X. He, A. A. Rockett, E. Eser, K. D. Dobson, R. W. Birkmire, *J. Appl. Phys.* **2017**, *121*, 245102.
[23] R. V. Forest, E. Eser, B. E. McCandless, J. G. Chen, R. W. Birkmire, *J. Appl. Phys.* **2015**, *117*, 115102.
[24] A. Rockett, J. S. Britt, T. Gillespie, C. Marshall, M. M. A. Jassim, F. Hasoon, R. Matson, B. Basol, *Thin Solid Films* **2000**, *372*, 212.
[25] S. Grini, K. V. Sopiha, N. Ross, X. Liu, T. S. Bjørheim, C. Platzer-Björkman, C. Persson, L. Vines, *Adv. Energy Mater.* **2019**, *9*, 1900740.
[26] M. Bär, B.-A. Schubert, B. Marsen, R. G. Wilks, S. Pookpanratana, M. Blum, S. Krause, T. Unold, W. Yang, L. Weinhardt, C. Heske, H.-W. Schock, *Appl. Phys. Lett.* **2011**, *99*, 222105.
[27] G. Brammertz, M. Buffière, S. Oueslati, H. ElAnzeery, K. Ben Messaoud, S. Sahayaraj, C. Köble, M. Meuris, J. Poortmans, *Appl. Phys. Lett.* **2013**, *103*, 163904.
[28] Y. Ren, J. J. S. Scragg, M. Edoff, J. K. Larsen, C. Platzer-Björkman, *ACS Appl. Mater. Interfaces* **2016**, *8*, 18600.
[29] T. Schwarz, O. Cojocaru-Mirédin, P. Choi, M. Mousel, A. Redinger, S. Siebentritt, D. Raabe, *Appl. Phys. Lett.* **2013**, *102*, 042101.
[30] T. Schwarz, O. Cojocaru-Mirédin, P. Choi, M. Mousel, A. Redinger, S. Siebentritt, D. Raabe, *J. Appl. Phys.* **2015**, *118*, 095302.
[31] T. Gershon, C. Hamann, M. Hopstaken, Y. S. Lee, B. Shin, R. Haight, *Adv. Energy Mater.* **2015**, *5*, 1500922.
[32] A. Stokes, M. Al-Jassim, D. Diercks, A. Clarke, B. Gorman, *Sci. Rep.* **2017**, *7*, 14163.
[33] M. Raghuwanshi, B. Thöner, P. Soni, M. Wuttig, R. Wuerz, O. Cojocaru-Mirédin, *ACS Appl. Mater. Interfaces* **2018**, *10*, 14759.
[34] C. Persson, A. Zunger, *Phys. Rev. Lett.* **2003**, *91*, 266401.
[35] A. Walsh, S. Chen, S.-H. Wei, X.-G. Gong, *Adv. Energy Mater.* **2012**, *2*, 400.
[36] A. Redinger, S. Siebentritt, *Appl. Phys. Lett.* **2010**, *97*, 092111.
[37] T. Schwarz, O. Cojocaru-Mirédin, M. Mousel, A. Redinger, D. Raabe, P. Choi, *Acta Mater.* **2017**, *132*, 276.
[38] E. S. Sanli, Q. M. Ramasse, R. Mainz, A. Weber, D. Abou-Ras, W. Sigle, P. A. van Aken, *Appl. Phys. Lett.* **2017**, *111*, 032103.
[39] C. Li, E. S. Sanli, H. Strange, M.-D. Heinemann, D. G. Schäfer, R. Mainz, W. Sigle, D. Abou-Ras, P. A. van Aken, *Microsc. Microanal.* **2018**, *24*, 1492.
[40] T. Abzieher, T. Schnabel, M. Hetterich, M. Powalla, E. Ahlswede, *Phys. Status Solidi A* **2016**, *213*, 1039.
[41] F. A. Stevie, C. W. Magee, R. G. Wilson, *Secondary Ion Mass Spectrometry: A Practical Handbook for Depth Profiling and Bulk Impurity Analysis*, Wiley, New York **1989**.
[42] R. V. Forest, E. Eser, B. E. McCandless, R. W. Birkmire, J. G. Chen, *AIChE J.* **2014**, *60*, 2365.
[43] B. Scherrer, M. V. F. Schlupp, D. Stender, J. Martynczuk, J. G. Grolig, H. Ma, P. Kocher, T. Lippert, M. Prestat, L. J. Gauckler, *Adv. Funct. Mater.* **2013**, *23*, 1957.
[44] S. Ø. Stub, E. Vøllestad, T. Norby, *J. Mater. Chem. A* **2018**, *6*, 8265.
[45] S. Ø. Stub, K. Thorshaug, P. M. Rørvik, T. Norby, E. Vøllestad, *Phys. Chem. Chem. Phys.* **2018**, *20*, 15653.
[46] S. Grini, N. Ross, C. Persson, C. Platzer-Björkman, L. Vines, *Thin Solid Films* **2018**, *665*, 159.
[47] K. Thompson, D. Lawrence, D. J. Larson, J. D. Olson, T. F. Kelly, B. Gorman, *Ultramicroscopy* **2007**, *107*, 131.
[48] *Atom Probe Microscopy* (Ed: B. Gault), Springer, New York **2012**.